Int j simul model 21 (2022) 2, 249-260
Original scientific paper

CAVITATION EROSION MODELLING – COMPARISON OF TWO SOLID ANGLE PROJECTION APPROACHES

Pezdevsek, M.[*]; Kevorkijan, L.[**] & Bilus, I.[**]
[*] University of Maribor, Faculty of Energy Technology, Hočevarjev trg 1, 8270 Krško, Slovenia
[**] University of Maribor, Faculty of Mechanical Engineering, Smetanova 17, 2000 Maribor, Slovenia
E-Mail: ignacijo.bilus@um.si

Abstract
In this paper we compared two different solid angle formulations to determine the amount of cavitation potential energy that is transfer from a source to a surface. The first formulation used an analytical expression for the solid angle of a planar triangle while the second formulation used a fully continuous form of the solid angle projection approach which represents the surface specific impact power at a point location. The comparison was conducted on a NACA 0018-45 hydrofoil. A block-structured computational mesh was created in ICEM CFD. Transient simulations were performed in Ansys CFX where the SST turbulence model with Reboud's correction was used. For the cavitation modelling the Schnerr-Sauer cavitation model with the recommended values was used. Result from Ansys CFX were imported into Matlab where the potential power applied to the surface was calculated for both formulations. The results of the study show that both formulations work well and predict similar locations where erosion occurred, the difference is in the absolute values which are significantly higher in the formulation that used the fully continuous form of the solid angle.
(Received in February 2022, accepted in April 2022. This paper was with the authors 2 weeks for 1 revision.)

Key Words: Cavitation, Erosion, Solid Angle, Numerical Simulation

1. INTRODUCTION

Cavitation is a phenomenon that occurs when a combination of low local static pressure and high velocities leads to pressures lower than the vapour pressure. Vapour structures occur in locations where the local pressure is below the vapour pressure.

In some areas cavitation can be beneficial, for example in the medical field for removal of kidney stones, however it is undesirable in engineering applications such as turbines, pumps, and rudders. Cavitation may cause deterioration in performance, vibrations and noise. Cavitation erosion occurs when the cavities collapse near the surface of a solid wall. Cavitation erosion is usually combined with other before mentioned unwanted cavitation effects.

The research of cavitation phenomenon dates to the late 19th and early 20th centuries. In 1917, Lord Rayleigh [1] derived the equation for calculation of the pressure in a liquid during the collapse of a spherical bubble. In 1949, Plesset [2] upgraded this work by writing the differential equation of the dynamics of a spherical bubble, today known as the Rayleigh-Plesset equation. Mostly experimental research of cavitation damage was conducted during the theoretical research of the cavitation phenomenon.

Hammit [3] studied cavitation damage on the case of fluid flow through a Venturi channel and introduced the erosion model based on the energy spectrum of a vapour cavity. Vogel et al. [4] observed the dynamics of the collapse of a bubble along a solid wall and derived the equation for calculation of the potential energy of the collapse.

By the end of the 20th century, two hypotheses were known about the origin of cavitation damage. The first hypothesis followed the high value of the pressure in the liquid around the bubble as it was calculated by Lord Rayleigh [1]. The existence of a pressure wave was confirmed by many experimental studies, for example, by Harrison [5]. A second, "microjet" hypothesis was proposed by Kornfeld and Suvorov [6], while Plesset and Chapman [7]

predicted the microjet velocity numerically and claimed that a microjet can damage the material.

Based on the pressure wave hypothesis, Fortes Patella et al. [8] presented an approach to erosion assessment with an energy cascade that transfers the initial potential energy of large vapour structures to the smallest structures, and eventually to the surface walls. A key contribution was the definition of the potential power of cavitation structures based on the total derivative of potential energy. The model upgrade is described in a paper of Leclercq et al. [9], where all of the vapour structures, even those not in direct contact with the wall, were considered. In the paper by Carrat et al. [10] the results of numerical analysis, including the amplitude and frequency of the pressure waves, were presented and validated experimentally. Based on their findings, Schenke and Terwisga [11] proposed a model of forecasting the erosion threat where energy generated by the vapour structures is conserved and transferred to the wall surface via the pressure wave released after the collapse. They also introduced a continuous formulation of energy transfer from wall-distant structures to the wall surface. Li [12] introduced the erosion intensity function, which is based on pressure only.

Hu et al. [13] investigated the influence of the inlet attack angle on the cavitation evolution of a low-specific-speed centrifugal pump. The incipient location of the cavitation appeared on the suction side of the leading edge of the blade close to the tongue. The cavitation at the tongue of a centrifugal pump at overload conditions was investigated in the paper by Hu et al. [14] where it was concluded that the cavitation at the tongue not only enhances the pressure fluctuation in the volute, but also affects the blade loading distribution.

2. GOVERNING EQUATIONS

In CFX the homogenous mixture flow is governed by the following set of equations, phases are considered incompressible and share the same velocity field $\boldsymbol{U}$. Continuity equation:

$$\nabla \cdot \boldsymbol{U} = \dot{m}\left(\frac{1}{\rho_\mathrm{l}} + \frac{1}{\rho_\mathrm{v}}\right) \tag{1}$$

where $\boldsymbol{U}$ is the time averaged mixture velocity, $\dot{m}$ is the interphase mass transfer rate due to cavitation, ρ_v is the vapour density and ρ_l is the liquid density.

Momentum equation for the liquid vapour mixture:

$$\frac{\partial(\rho \boldsymbol{U})}{\partial t} + \nabla \cdot (\rho \boldsymbol{U}\boldsymbol{U}) = -\nabla p + \nabla \cdot \left((\mu + \mu_\mathrm{t})(\nabla \boldsymbol{U} + (\nabla \boldsymbol{U})^T)\right) \tag{2}$$

where ρ is the density of the water-vapour mixture, p is the time averaged pressure, μ is the dynamic viscosity of the water-vapour mixture and μ_t is the turbulent viscosity.

Volume fraction equation for the liquid phase is defined as:

$$\frac{\partial \gamma}{\partial t} + \nabla \cdot (\gamma \boldsymbol{U}) = \frac{\dot{m}}{\rho_\mathrm{l}} \tag{3}$$

where γ is the water volume fraction.

The water volume fraction γ and vapour volume fraction α are defined as:

$$\gamma = \frac{\text{liquid volume}}{\text{total volume}};\ \alpha = \frac{\text{vapour volume}}{\text{total volume}} \tag{4}$$

2.1 Turbulence model

The SST turbulence model was proposed by Menter [15] and is a blend between the *k*-ω model for the region near the surface and *k*-ε model for the outer region. The model consists of a transformation of the *k*-ε model to a *k*-ω formulation. This is achieved by using a blending function F_1. F_1 is equal to one near the surface and decreases to a value of zero outside the

boundary layer. The turbulent viscosity is modified to account for the transport of the turbulent shear stress. The turbulent viscosity is defined as:

$$\mu_t = \frac{\rho\, a_1 k}{\max(a_1\omega, SF_2)} \tag{5}$$

where k is the turbulent kinetic energy, ω is the specific dissipation rate, S is the strain rate magnitude, a_1 is the constant (0.31 [15]) and F_2 is the second blending function.

Two-equation turbulence models were developed for single phase flows, they tend to overestimate the turbulent viscosity in the region of transition between vapour and liquid phase and damp the unsteadiness of the cavitating regime [12].

Reboud et al. [16] proposed a modification of the k-ε turbulence model by reducing the turbulent viscosity in order to take into account the suggested two-phase flow effects on the turbulent structures [12]. The density in the turbulent viscosity equation is now replaced with a density function and is written as:

$$f(\rho) = \rho_\mathrm{v} + \frac{(\rho - \rho_\mathrm{v})^n}{(\rho_\mathrm{l} - \rho_\mathrm{v})^{n-1}} \tag{6}$$

where ρ is the mixture density and n is a constant (10 [12]).

2.2 Cavitation model

Schnerr and Sauer [17] assumed that the vapour structure is filled with spherical bubbles which are governed by the simplified Rayleigh-Plesset equation. The mass transfer rate in the Schnerr and Sauer model is proportional to $\alpha(1-\alpha)$:

$$\dot{m} = \begin{cases} F_\mathrm{vap}\dfrac{\rho_\mathrm{v}\rho_\mathrm{l}}{\rho}\alpha(1-\alpha)\dfrac{3}{R_\mathrm{B}}\sqrt{\dfrac{2}{3}\dfrac{p_\mathrm{v}-p}{\rho_\mathrm{l}}} & \text{if } p < p_\mathrm{v} \\ F_\mathrm{cond}\dfrac{\rho_\mathrm{v}\rho_\mathrm{l}}{\rho}\alpha(1-\alpha)\dfrac{3}{R_\mathrm{B}}\sqrt{\dfrac{2}{3}\dfrac{p-p_\mathrm{v}}{\rho_\mathrm{l}}} & \text{if } p > p_\mathrm{v} \end{cases} \tag{7}$$

where p_v is the vapour saturation pressure, R_B is the bubble radius, F_vap is the evaporation coefficient and F_cond is the condensation coefficient.

The bubble radius is defined as:

$$R_\mathrm{B} = \left(\frac{\alpha}{1-\alpha}\frac{3}{4\pi n_\mathrm{B}}\right)^{\frac{1}{3}} \tag{8}$$

where n_B is the bubble number density. The recommended values for the two coefficients are $F_\mathrm{vap} = 1$ and $F_\mathrm{cond} = 0.2$. The recommended value for the bubble number density is $n_\mathrm{B} = 10^{13}$ [12].

2.3 Cavitation erosion potential

Based on the work of [9, 18], we can calculate the potential energy of vapour structures E_pot as:

$$E_\mathrm{pot} = (p - p_\mathrm{v})V_\mathrm{v} \tag{9}$$

where V_v is the volume of the vapour structure.

The potential power of vapour structures P_pot for each cell can be separated in two terms, the first term takes into account the contribution of the void fraction derivative and the second term that takes into account the pressure derivative:

$$\frac{P_{\text{pot}}}{V_{\text{cell}}} = -\frac{1}{V_{\text{cell}}}\frac{dE_{\text{pot}}}{dt} = \frac{P_{\text{pot}}|_{p=\text{const.}}}{V_{\text{cell}}} + \frac{P_{\text{pot}}|_{\alpha=\text{const.}}}{V_{\text{cell}}} \tag{10}$$

where V_{cell} is the volume of an element. For the void fraction derivative term the potential power is defined as:

$$P_{\text{pot}}|_{p=\text{const.}} = -(p - p_{\text{v}})\left(\frac{dV_{\text{v}}}{dt}\right) \tag{11}$$

The negative sign is needed to obtain a positive value for the instantaneous potential power, as only a reduction in cavitation erosion potential represents vapour cavity collapse, and only the collapse stage is considered in the model. We assume that the vapour structure is aggressive if $P_{\text{pot}} > 0$.

The potential power density is defined as:

$$\frac{P_{\text{pot}}|_{p=\text{const.}}}{V_{\text{cell}}} = -(p - p_{\text{v}})\left(\frac{d\alpha}{dt}\right) \tag{12}$$

Inside the volume of an element V_{cell} the vapour fraction is defined as:

$$\alpha = \frac{V_{\text{v}}}{V_{\text{cell}}} = \frac{\rho}{\rho_{\text{l}} - \rho_{\text{v}}} \tag{13}$$

If we take into account the Lagrangian time derivative:

$$\frac{d\rho}{dt} + \rho\ \text{div}(\boldsymbol{U}) = 0 \tag{14}$$

From this we can conclude:

$$\frac{P_{\text{pot}}|_{p=\text{const.}}}{V_{\text{cell}}} = -(p - p_{\text{v}})\frac{\rho}{\rho_{\text{l}} - \rho_{\text{v}}}\ \text{div}(\boldsymbol{U}) \tag{15}$$

For the pressure derivative term the potential power is defined as:

$$\frac{P_{\text{pot}}|_{\alpha=\text{const.}}}{V_{\text{cell}}} = -\alpha\left(\frac{\partial p}{\partial t} + \boldsymbol{U}\cdot\text{grad}(p)\right) \tag{16}$$

We calculated both terms and came to the same conclusion as the other authors [9, 19] that the void derivative term is dominant $\left\|P_{\text{pot}}|_{\alpha=\text{const.}}\right\| \ll \left\|P_{\text{pot}}|_{p=\text{const.}}\right\|$ and so the pressure derivative term can be ignored.

2.4 Solid angle

The solid angle Ω is defined as the area that an element projects on a sphere divided by the radius of the sphere (see Fig. 1).

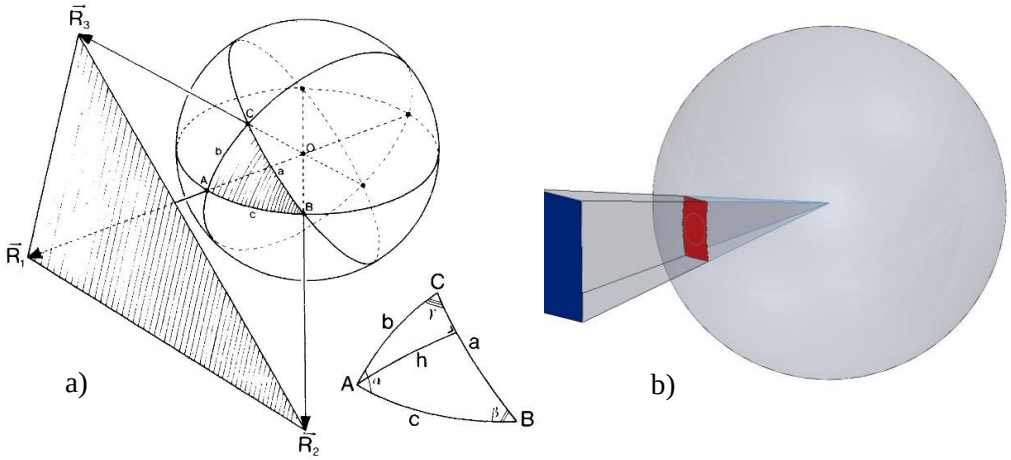

Figure 1: a) solid angle for a planar triangle [20], b) solid angle for a quadrilateral surface.

It is essentially a measure of the amount of the field of view and in our case it will quantify the distance and angle from an energy source to the surface element:

$$\Omega = \frac{A}{r^2} \tag{17}$$

where A is the area on the sphere and r is the sphere radius.

The analytical expression for the solid angle of a planar triangle was derived in [20] and is written as:

$$\tan\left(\frac{1}{2}\Omega\right) = \frac{\overrightarrow{R_1}\cdot\left(\overrightarrow{R_2}\times\overrightarrow{R_3}\right)}{R_1R_2R_3 + \left(\overrightarrow{R_1}\cdot\overrightarrow{R_2}\right)R_3 + \left(\overrightarrow{R_1}\cdot\overrightarrow{R_3}\right)R_2 + \left(\overrightarrow{R_2}\cdot\overrightarrow{R_3}\right)R_1} \tag{18}$$

Leclerq et al. [9] used the above form to employ the solid angle to project the radiated power on a triangular surface element. Schenke et al. [21] used a different approach with a fully continuous form of the solid angle projection approach was, which represents the surface specific impact power at a point location and is defined as:

$$\Omega = \frac{(\vec{x}_{\text{cell}} - \vec{x}_{\text{S}})\cdot\vec{n}}{|\vec{x}_{\text{cell}} - \vec{x}_{\text{S}}|^3} \tag{19}$$

Both formulations represent an energy conservative conversion of the potential power (see Fig. 2).

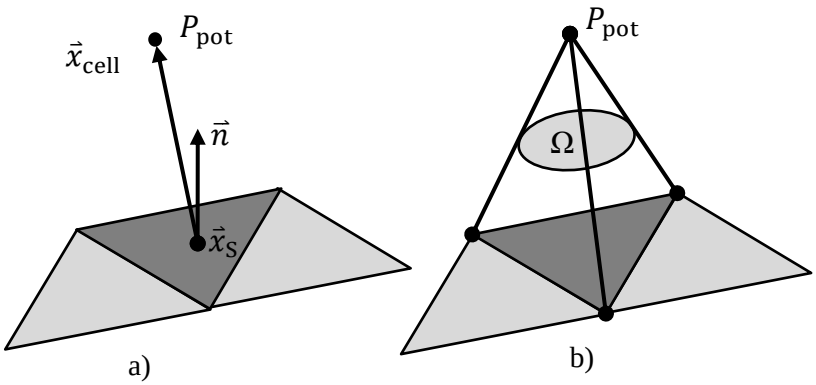

Figure 2: a) fully continuous form of the solid angle, b) an illustration of the solid angle projection.

2.5 Potential power applied to the surface

Based on the work in [22] and [9] we can define the potential power applied to each surface element j and for all volume elements i as:

$$\frac{P_{\text{mat}_\text{j}}}{\Delta S_\text{j}} = \frac{1}{\Delta S_\text{j}} \sum_{i|\overrightarrow{Xs_\text{j}Xcell_\text{i}}\cdot\overrightarrow{n_\text{j}}>0} \frac{\Omega_{\text{ij}}}{4\pi} P_{\text{pot}_\text{i}} \tag{20}$$

where ΔS_j is the area of a surface element, $\overrightarrow{Xs_\text{j}Xcell_\text{i}}$ is the vector from the centre of the surface element j to the centre of the volume element i and $\overrightarrow{n_\text{j}}$ is the normal vector of the surface element j.

We can then add up all the potential power applied to each surface for all the time steps and then divide by the number of time steps to get the mean loading $P_{\text{mean,mat}}$ which represent a qualitative representation of the eroded region:

$$\frac{P_{\text{mean,mat}}}{\Delta S_\text{j}} = \frac{1}{N}\sum_{i=1}^{N}\frac{P_{\text{mat}_\text{j}}}{\Delta S_\text{j}} \tag{21}$$

3. NUMERICAL TEST CASE AND SETUP

3.1 Geometry

The hydrodynamic profile NACA 0018-45 was chosen for this study, it is a modified four digit NACA 0018 profile which is indicated by the 45 digits. The chord length for the profile was defined at 60 mm and an angle of attack of 6.5 °. The size of the computational domain was 2 chord lengths before the leading edge, 5 chord lengths after the leading edge and the height of the domain was 1.33 chord lengths. The width of the domain was set at 40 mm.

3.2 Mesh

For this study a block-structured mesh was created in ICEM CFD. The geometry of the hydrodynamic profile was defined with 214 elements while the whole profile surface had 7200 elements. The final mesh had approximately 765.000 elements. For the elements near the profile surface the condition y+ < 1 was prioritised (see Fig. 3).

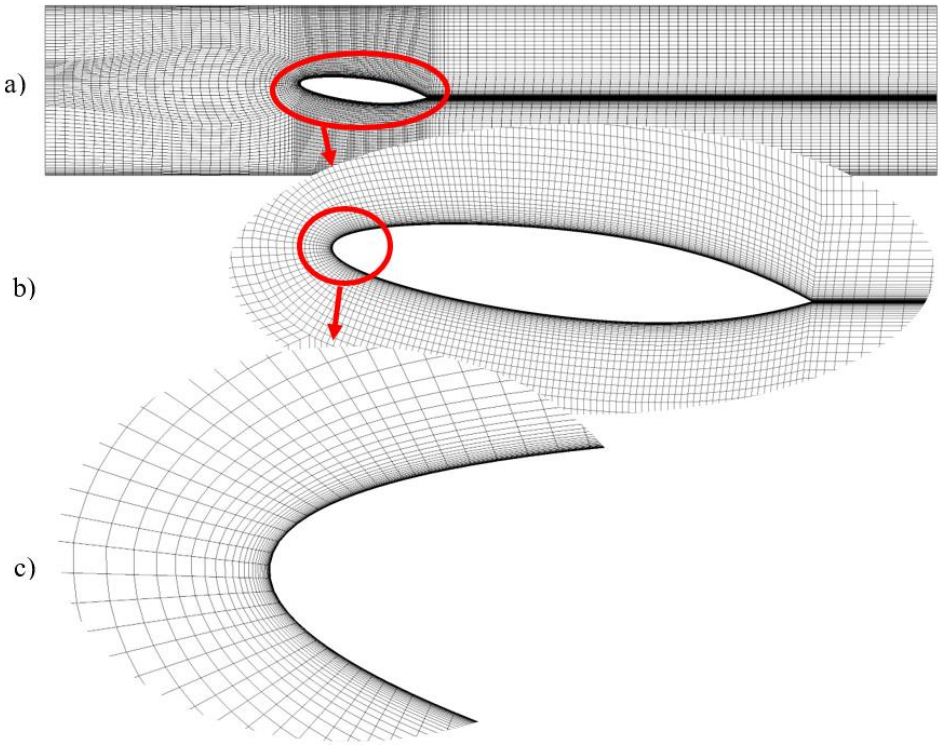

Figure 3: a) surface mesh of the whole domain, b) a cropped area of the mesh, c) a close up of the leading edge.

3.3 Boundary conditions

The left surface was defined as an inlet with a normal velocity of 24.2 m/s. The right surface was defined as an outlet with a static pressure of 213.115 kPa. The bottom, top, side surfaces and the surface of the hydrodynamic profile were defined as no slip walls.

Transient simulations were conducted in Ansys CFX. The time step for the simulation was defined as 10^{-5} s. The convergence criterion for the RMS residuals was defined as 10^{-6}. We defined the maximum number of iterations within a time step at 50. The SST turbulence model was used with the Reboud's correction. For the Schnerr-Sauer cavitation model the default values for the coefficients were used. The vapour saturation pressure (p_v) was set at 2811 Pa.

Results from Ansys CFX 2020 R2 were imported into Matlab 2021b where we calculated the mean potential power applied to each surface element.

4. RESULTS

The total vapour volume in the computational domain is shown in Fig. 4 for the time interval 0 s to 0.08 s. From the figure we can see that the total vapour volume in the domain changes periodically, which confirms the transient nature of the extent of cavitation. Within the simulated time multiple vapour cloud shedding events occurred, which allowed for a consistent analysis of cavitation erosion.

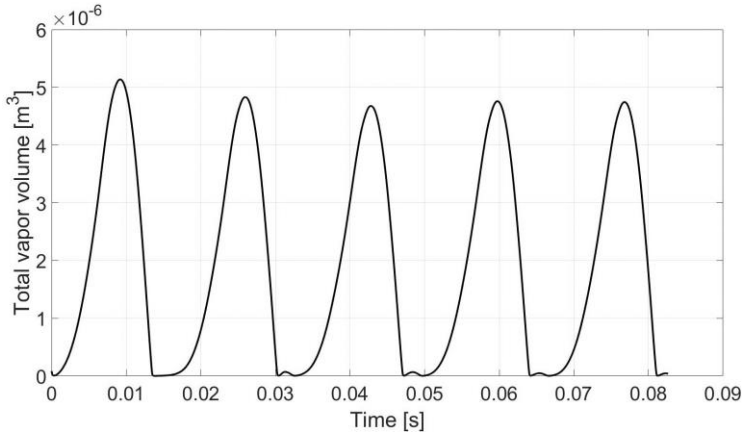

Figure 4: Total vapour volume in the domain.

Based on the data from Fig. 4 we conducted a FFT analysis. The results show (see Fig. 5) a regular harmonic variation at a frequency of 59 Hz, which is comparable to results from literature [12].

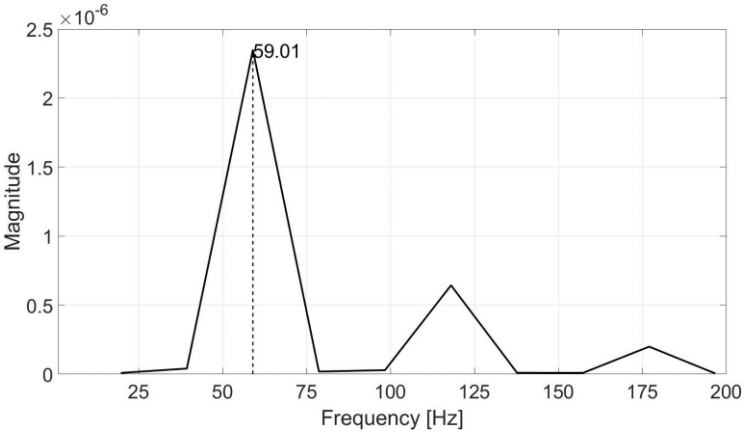

Figure 5: Spectral analysis of the time history of the total vapour volume.

Based on the result seen in Fig. 6 the unsteady dynamics occur on the suction side as well as on the pressure side. The collapses mostly occur near the trailing edge, suggesting that high impacts are likely to occur in the trailing edge region. The basic phenomena during one shedding cycle can be characterized by the following 12 instantaneous plots of the iso-surface of $\alpha = 0.1$.

- On the suction side a sheet cavity develops from the leading edge of the hydrofoil and continues to grow ①②.
- The sheet cavity continues to grow on the suction side to about 90 % of the chord length③④⑤.
- Vapour structures begin to form around the middle of the hydrofoil ⑥⑦.
- The vapour structure begins shedding from the main cavity ⑧⑨, simultaneously on the pressure side small vapour structures are formed.

- The vapour structure detaches from the main cavity and collapses near the trailing edge, the suction side sheet cavity retreats towards the leading edge ⑩⑪.
- The sheet has disappeared and one cycle is finished ⑫.

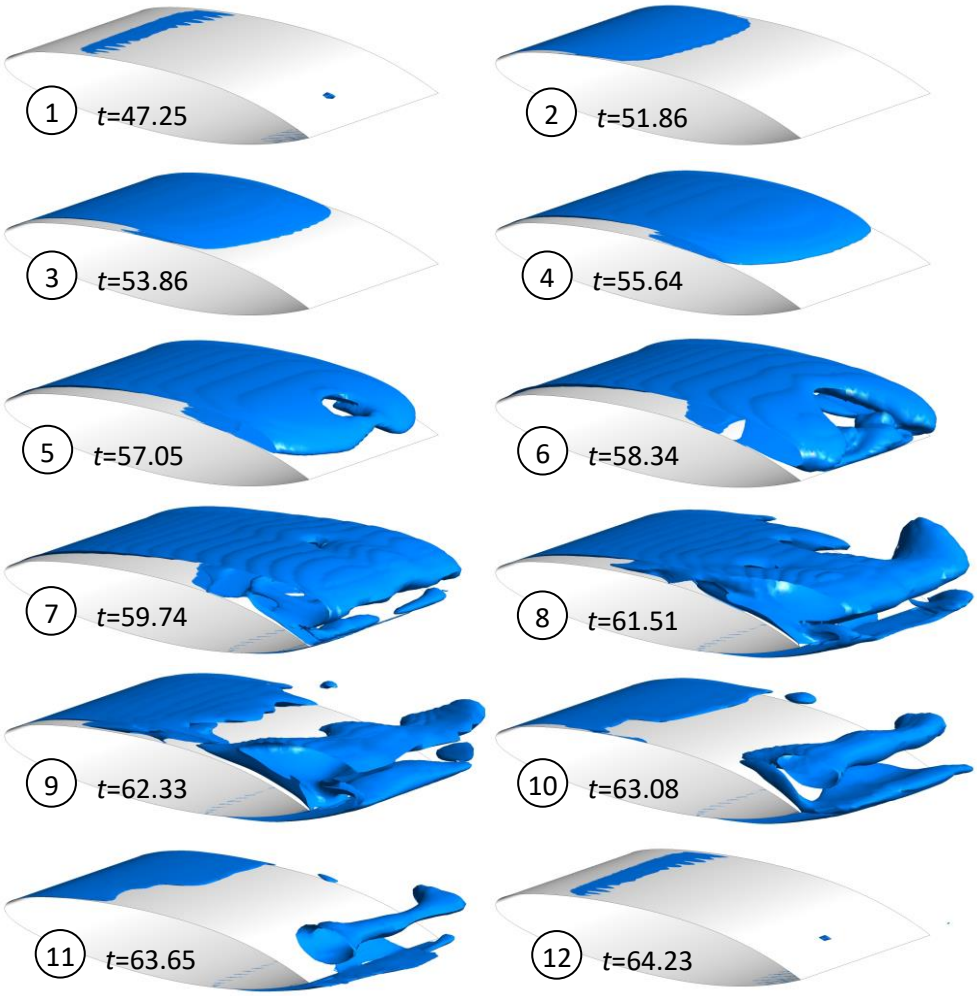

Figure 6: Sequences of iso-surface plots of instantaneous vapour volume fraction of α = 0.1 during one typical shedding cycle.

The sequences of iso-surface plots that were shown in the previous figure are also represented in Fig. 7 where the locations are marked on a graph of the total vapour volume in dependence of time.

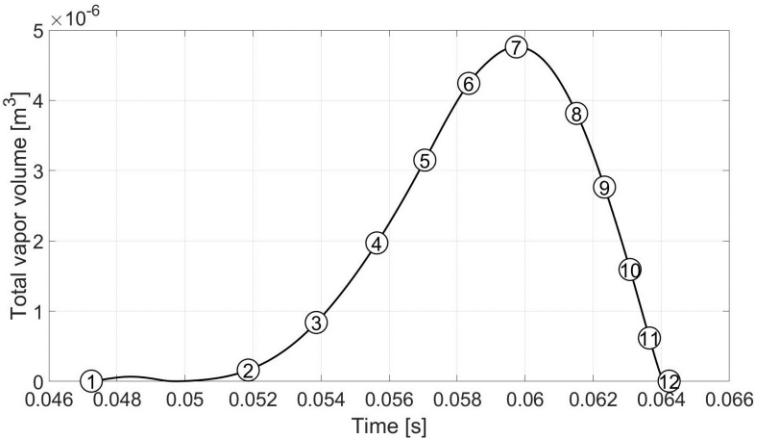

Figure 7: One shedding cycle with marked sequences of iso-surface plots.

Fig. 8 shows a plot of the solid angle for both the formulation used by Leclercq et al. and the formulation used by Schenke et al. The plot was limited for solid angles between 0 and 0.1 sr, so we can better compare the distribution for both methods. The black square represents the chosen surface element. From the results in Fig. 8 we can conclude that the distribution for both methods looks very similar.

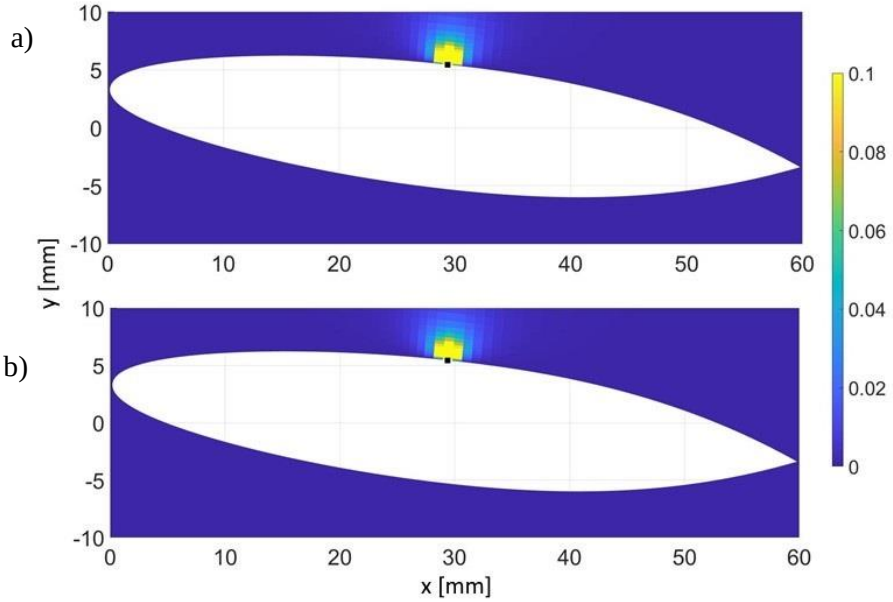

Figure 8: Solid angle values for a) the method by Leclerq et al., b) the method by Schenke et al.

Fig. 9 shows a plot of the solid angle for both the formulation used by Leclercq et al. and the formulation used by Schenke et al. The plot was limited for solid angles between 1 – 10 sr and focused on solid angle values near the surface. The black square represents the chosen surface element. From the results in Fig. 9 we see that near the selected surface element the solid angle values differ and are higher in the formulation used by Schenke et al. The maximum solid angle value is at the element nearest to the selected surface element. For the formulation used by Schenke et al. the maximum solid angle value is 116610 sr. While the maximum value for the formulation used by Leclerq et al. is 6.24 sr, which is considerably lower.

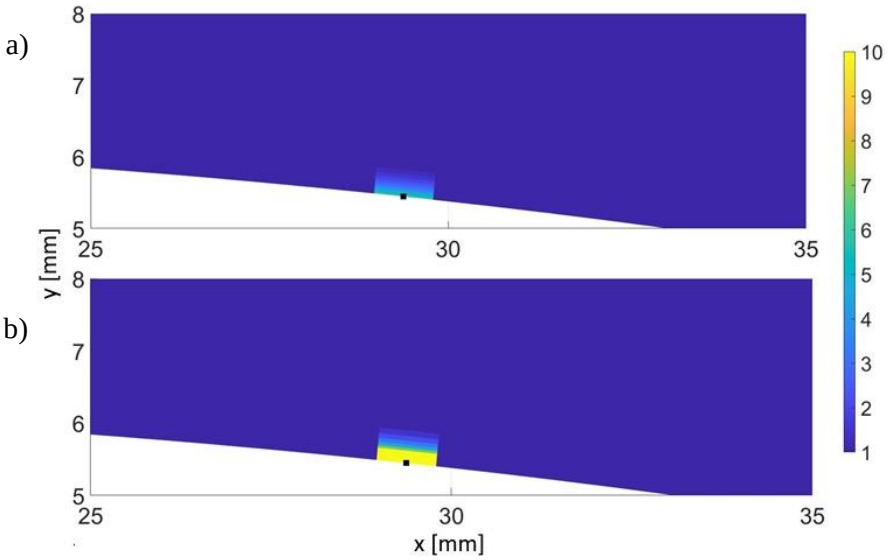

Figure 9: The figure shows solid angle values near the surface for a) the method used by Leclerq et al., b) the method used by Schenke et al.

In Fig. 10 we see the mean potential power applied to the top surface of the hydrofoil for the formulation used by Leclerq et al. The locations with the highest values of the mean potential power applied to the surface are at the trailing edge which is in agreement with experimental results from literature [12]. In experimental results [12] from literature the erosion area was largely found on the trailing edge and in a smaller amount near the middle of the hydrofoil, which we did not see in our study.

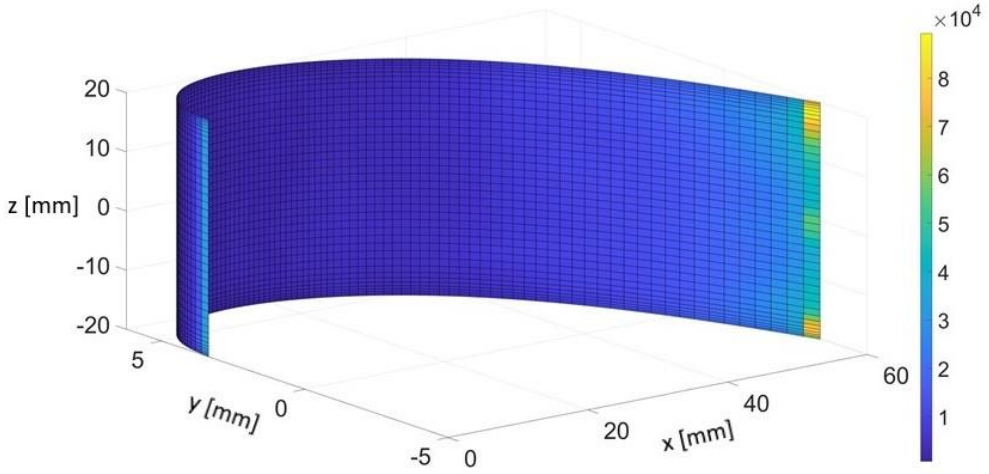

Figure 10: Mean potential power applied to the top surface of the hydrofoil [W/m^2] for the formulation used by Leclerq et al.

In Fig. 11 we see the mean potential power applied to the surface for the formulation used by Shenke et al. The locations with the highest values of the mean potential power applied to the surface are at the trailing edge which is in agreement with experimental results from literature [12]. The locations with the highest values of the mean potential power applied to the surface do not differ significantly for both formulations. The difference is in the absolute values which are significantly higher in the formulation that used by Shenke et al.

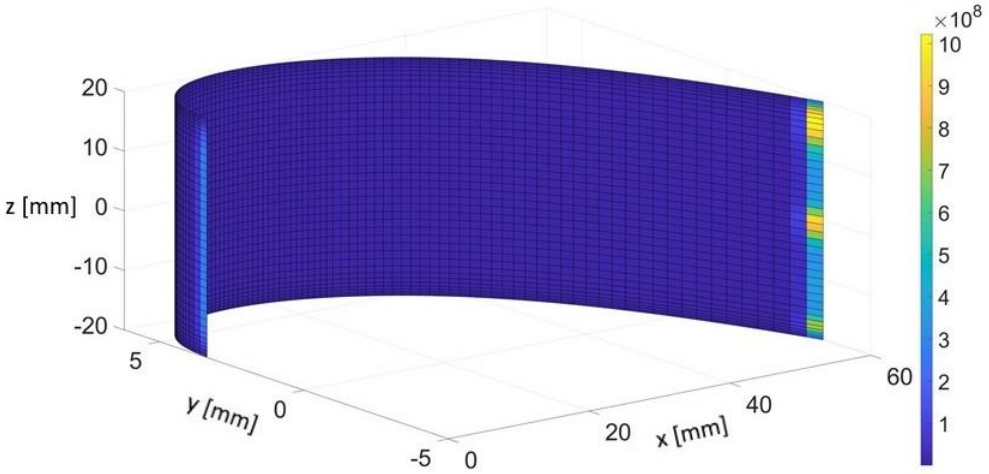

Figure 11: Mean potential power applied to the top surface of the hydrofoil [W/m^2] for the formulation used by Shenke et al.

5. CONCLUSION

Transient simulations were performed in Ansys CFX with a time step of 10^{-5} s. From the simulation data we saw that the total vapour volume in the domain changes periodically, which confirms the transient nature of the extent of cavitation. Within the simulated time of 0.08 s multiple vapour cloud shedding events occurred, which allowed for a consistent analysis of

cavitation erosion. An FFT analysis was done on the total vapour volume data and the shedding frequency was calculated at 59 Hz, which is similar to results from literature [12].

An appropriate description of cavitation dynamics is crucial. The Schnerr-Sauer cavitation model predicts the extent and dynamics of cavitation correctly. Based on the results the vapour structure collapses happened at or near the trailing edge so we can expect the cavitation erosion to be the highest at that location.

Result from the transient simulation in Ansys CFX were imported into Matlab where the mean potential power applied to the surface was calculated for both solid angle formulations. The applied model transfers potential energy from cavitation structures to the surface, is energy conservative, which makes it a good basis for predicting the response of various materials exposed to the phenomenon of cavitation.

The distribution for both formulations of the solid angle look very similar, while the solid angle values are also similar for elements that are not near the selected surface element. For solid angle values near the selected surface element there is a large discrepancy between the two formulations. For the formulation used by Schenke et al. the maximum solid angle value was 116610 sr. While the maximum value for the formulation used by Leclerq et al. is 6.24 sr, which is considerably lower.

Based on solid angle values we can estimate that the mean potential power applied to the surface will also be larger for the formulation used by Schenke et al., which is confirmed by our results. The locations with the highest values of the mean potential power applied to the surface are at the trailing edge and do not differ significantly for both formulations. Both formulations show good agreement with experimental results from literature [12], where the erosion area was largely found on the trailing edge and in a smaller amount near the middle of the hydrofoil, which we did not see in our study. In future work we can improve upon the study by adding a prediction for the cavitation erosion rate, which would require experimental verification and additional model calibration to correctly implement.

REFERENCES

[1] Lord Rayleigh, O. M. F. R. S. (1917). VIII. On the pressure developed in a liquid during the collapse of a spherical cavity, *The London, Edinburgh, and Dublin Philosophical Magazine and Journal of Science*, Vol. 34, No. 200, 94-98, doi:10.1080/14786440808635681

[2] Plesset, M. S. (1949). The dynamics of cavitation bubbles, *Journal of Applied Mechanics*, Vol. 16, No. 3, 277-282, doi:10.1115/1.4009975

[3] Hammitt, F. G. (1963). Observations on cavitation damage in a flowing system, *Journal of Basic Engineering*, Vol. 85, No. 3, 347-356, doi:10.1115/1.3656601

[4] Vogel, A.; Lauterborn, W.; Timm, R. (1989). Optical and acoustic investigations of the dynamics of laser-produced cavitation bubbles near a solid boundary, *Journal of Fluid Mechanics*, Vol. 206, 299-338, doi:10.1017/S0022112089002314

[5] Harrison, M. (1952). An experimental study of single bubble cavitation noise, *The Journal of the Acoustical Society of America*, Vol. 24, No. 4, Program of the 43rd Meeting of the Acoustical Society of America, Session G. Ultrasonics and Underwater Sound, 454, G4, doi:10.1121/1.1917513

[6] Kornfeld, M.; Suvorov, L. (1944). On the destructive action of cavitation, *Journal of Applied Physics*, Vol. 15, No. 6, 495-506, doi:10.1063/1.1707461

[7] Plesset, M. S.; Chapman, R. B. (1971). Collapse of an initially spherical vapour cavity in the neighbourhood of a solid boundary, *Journal of Fluid Mechanics*, Vol. 47, No. 2, 283-290, doi:10.1017/S0022112071001058

[8] Fortes-Patella, R.; Reboud, J.-L.; Briançon-Marjollet, L. (2004). A phenomenological and numerical model for scaling the flow aggressiveness in cavitation erosion, *Cavitation Erosion Workshop*, 36 pages

[9] Leclercq, C.; Archer, A.; Fortes-Patella, R.; Cerru, F. (2017). Numerical cavitation intensity on a hydrofoil for 3D homogeneous unsteady viscous flows, *International Journal of Fluid Machinery and Systems*, Vol. 10, No. 3, 254-263, doi:10.5293/IJFMS.2017.10.3.254

[10] Carrat, J.-B.; Fortes-Patella, R.; Franc, J.-P. (2019). Experimental and numerical investigation of the erosive potential of a leading edge cavity, *International Journal of Fluid Machinery and Systems*, Vol. 12, No. 2, 136-146, doi:10.5293/IJFMS.2019.12.2.136

[11] Schenke, S.; van Terwisga, T. J. C. (2019). An energy conservative method to predict the erosive aggressiveness of collapsing cavitating structures and cavitating flows from numerical simulations, *International Journal of Multiphase Flow*, Vol. 111, 200-218, doi:10.1016/j.ijmultiphaseflow.2018.11.016

[12] Li, Z. R. (2012). Assessment of cavitation erosion with a multiphase Reynolds-averaged Navier-Stokes method, PhD Thesis, TU Delft, Delft

[13] Hu, Q. X.; Yang, Y.; Shi, W. D. (2020). Cavitation simulation of centrifugal pump with different inlet attack angles, *International Journal of Simulation Modelling*, Vol. 19, No. 2, 279-290, doi:10.2507/IJSIMM19-2-516

[14] Hu, Q.; Yang, Y.; Cao, W. (2020). Computational analysis of cavitation at the tongue of the volute of a centrifugal pump at overload conditions, *Advances in Production Engineering & Management*, Vol. 15, No. 3, 295-306, doi:10.14743/apem2020.3.366

[15] Menter, F. R. (1994). Two-equation eddy-viscosity turbulence models for engineering applications, *AIAA Journal*, Vol. 32, No. 8, 1598-1605, doi:10.2514/3.12149

[16] Reboud, J.-L.; Stutz, B.; Coutier-Delgosha, O. (1998). Two phase flow structure of cavitation: experiment and modelling of unsteady effects, *Proceedings of the 3rd International Symposium on Cavitation*, 7 pages

[17] Schnerr, G. H.; Sauer, J. (2001). Physical and numerical modelling of unsteady cavitation dynamics, *4th International Conference on Multiphase Flow*, 12 pages

[18] Pereira, F. (1997). Prédiction de l'érosion de cavitation: approche énergétique, PhD Thesis, Ecole Polytechnique Federale de Lausanne, Lausanne

[19] Fortes-Patella, R.; Archer, A.; Flageul, C. (2012). Numerical and experimental investigations on cavitation erosion, *IOP Conference Series: Earth and Environmental Science*, Vol. 15, Paper 022013, 12 pages, doi:10.1088/1755-1315/15/2/022013

[20] Van Oosterom, A.; Strackee, J. (1983). The solid angle of a plane triangle, *IEEE Transactions on Biomedical Engineering* , Vol. BME-30, No. 2, 125-126, doi:10.1109/tbme.1983.325207

[21] Schenke, S.; Melissaris, T.; van Terwisga, T. J. C. (2019). On the relevance of kinematics for cavitation implosion loads, *Physics of Fluids*, Vol. 31, No. 5, Paper 052102, 15 pages, doi:10.1063/1.5092711

[22] Krumenacker, L.; Fortes-Patella, R.; Archer, A. (2014). Numerical estimation of cavitation intensity, *IOP Conference Series: Earth and Environmental Science*, Vol. 22, Paper 052014, 11 pages, doi:10.1088/1755-1315/22/5/052014